Int J Fract (2014) 189:149–162
DOI 10.1007/s10704-014-9967-z

ORIGINAL PAPER

A study of frictional contact in dynamic fracture along bimaterial interfaces

Fabian Barras · David S. Kammer · Philippe H. Geubelle · Jean-François Molinari

Received: 24 March 2014 / Accepted: 11 August 2014 / Published online: 29 August 2014

Abstract We investigate numerically the dynamic in-plane propagation of a centered crack along bimaterial interfaces using a spectral formulation of the elastodynamic boundary integral equations. Particular attention is given to the effect of contact zones at the subsonic/intersonic transition. In a single set-up, we simulate and describe the different phenomenon observed experimentally (distinct natures of contact zones, unfavorable velocity range, asymmetric crack propagation). We show that different behaviors are observed as function of the crack propagation direction, i.e., with respect to the particle displacements of the compliant material. When the crack propagates in the same direction, the propagation velocities between c_R and c_s are forbidden and the subsonic/intersonic transition occurs with the nucleation of a daughter crack in front of the main rupture. The intersonic stress field at the crack front is compressive due to the material mismatch and a contact zone appears behind the tip. In the opposite direction, a smooth subsonic/intersonic transition occurs although crack face closure (in normal direction) is observed for speeds between c_s and $\sqrt{2}c_s$. In this regime, a Rayleigh disturbance is generated at the crack surface causing a contact zone which detaches from the tip. Using a contact model governed by a regularized Coulomb law, we provide a quantitative evaluation of the influence of friction on the effective fracture toughness. Finally, we show the applicability of our analysis to the description of different bimaterial situations as well as the single-material set-up.

Keywords Dynamic fracture · Intersonic crack propagation · Friction · Bimaterial interface · Boundary integral method

F. Barras · D. S. Kammer · J.-F. Molinari (✉)
IIC-ENAC, IMX-STI, Computational Solid Mechanics Laboratory (LSMS), Ecole Polytechnique Fédérale de Lausanne (EPFL), Station 18, 1015 Lausanne, Switzerland
e-mail: jean-francois.molinari@epfl.ch

F. Barras · P. H. Geubelle
Department of Aerospace Engineering, University of Illinois at Urbana-Champaign, 306 Talbot Laboratory, 104 South Wright Street, Urbana, IL 61801, USA

1 Introduction

Intersonic debonding, for which the speed of the front exceeds the shear wave speed of the material, has received increasing attention over the past two decades. Although intersonic crack growth was thought to be unattainable for a while, it is now acknowledged that it plays an important role in interface failure of multi-phase materials, composites or geophysical layers.

Experiments of crack propagation in homogeneous brittle solids measured crack propagations always slower than 65 % of the material's Rayleigh wave speed c_R (Rosakis 2002). Observed cracks were purely mode-I and their propagation speeds were often limited by branching. Singular dynamic fracture models (i.e., in which there is a stress singularity at the

sharp crack tip) also showed that super-Rayleigh crack growth is unreachable in homogeneous elastic solids. For instance, Freund (1990) showed that the energy flux into the tip of a remotely loaded crack decreases as the crack accelerates, and vanishes at a velocity equal to c_R.

However, these limitations are removed when crack branching and kinking is prevented by the existence of a weak plane of propagation where the fracture toughness is lower than in the surrounding solids. When the crack is trapped into a plane of propagation, it is usually mixed mode, which allows for a higher propagation speed. Freund (1979) studied the dynamic propagation of sharp mode-II cracks at weak interfaces. His analytical work demonstrated that the energy release rate is nonzero only at speed $\sqrt{2}c_s$ or sub-Rayleigh regimes for which the stress field is square root singular at the crack tip. Other intersonic speeds present a zero energy release rate which was not a sufficient proof of their existence. However when the rupture is not considered to be singular but smeared out in space and time within a cohesive zone, both analytical (Broberg 1989) and numerical (Andrews 1976) models showed that every intersonic mode-II crack speed is physically admissible.

The first experimental evidence of an intersonic crack propagation in a homogeneous material was provided by Rosakis et al. (1999). To avoid energetic dissipation by branching or micro-cracking, a weak plane of propagation was created by bonding two plates of Homalite together. A pre-notch crack at the edge of the interface was loaded by a lateral impact, while crack propagation was monitored using high speed photoelasticity. Coker and Rosakis (2001) also studied crack propagation in unidirectional graphite–epoxy composite plates. If under mode-I loading the recorded speeds were bounded at c_R, the authors observed intersonic crack propagations for mode-II loading conditions. The role of crack velocity on the cohesive failure along a single-material interface was studied by Kubair et al. (2002). Their analytical work showed that the cohesive damage is purely shear when the crack is intersonic, even for mixed mode loadings. In parallel to steady-state models, numerical simulations provided the opportunity to study the transition from subsonic to intersonic speeds. Needleman (1999) observed that the crack speed jumps from values close to c_R up to a regime between $\sqrt{2}c_s$ and the P-wave speed c_p.

Before these observations at single-material interfaces, it was already known that between dissimilar materials, crack can propagate intersonically with respect to the compliant medium. Lambros and Rosakis (1995) showed the first experimental proof of an intersonic crack propagation along a straight-line weak interface between PMMA and steel plates. Moreover, between two dissimilar materials, the presence of large scale contact zones after failure is a new feature of intersonic crack growth. Liu et al. (1995) derived the asymptotic solution for intersonic crack growth at the interface between an elastic solid and a rigid substrate. The asymptotic model shows that when the crack speed is between the shear wave speed of the elastic medium c_s and $\sqrt{2}c_s$, the normal stress ahead of the crack front has the opposite sign of the normal displacement behind it, i.e., with a tensile loading, a face closure is predicted behind the crack tip. The authors concluded that this regime might cause the presence of large scale contact during intersonic debonding and is unfavorable for stable crack growth. Beside this theoretical work, several experiments (Singh et al. 1997; Rosakis et al. 1998; Samudrala and Rosakis 2003) were conduced along interfaces bonding a very stiff body (Steel or Aluminium) to a more compliant material (PMMA or Homalite) revealing the presence of large scale contact zones behind intersonic ruptures. By adding a trailing contact zone of finite length to Liu's asymptotic solution, Huang et al. (1998) were able to reproduce the main experimental observations. Moreover, the presence of compressive normal stress along part of the interface associated with intersonic crack growth is also observed in numerical simulations of bimaterial debonding (Xu and Needleman 1996; Needleman and Rosakis 1999; Hao et al. 2004). Even though these numerical models did not account for real contact conditions between crack faces, the presence of this compressive stress field confirms the ability of large scale contact zones to develop along bimaterial interfaces. If the presence of contact is now obvious in intersonic crack propagation, its effect on the fracture process and the crack propagation is still overlooked. Subsequent experiments confirmed that the behavior of those large scale contact zones is little understood. Between a polymer and a very stiff body, Samudrala and Rosakis (2003) observed two distinct contact behaviors. Depending on the applied loading, the contact zone either trailed the crack tip or detached from the front and had its own leading and

trailing edges. Along composite-Homalite interfaces, Coker et al. (2003) showed experimentally and numerically that the crack speed regime also varies as a function of crack growth direction with respect to particle displacement. The effect of the propagation direction was also observed numerically at frictional interfaces (Kammer et al. 2012).

In this context, the purpose of this work is the numerical study of the behavior and the role of large scale contact zones appearing at intersonic debonding. The effect of the applied loading and the material mismatch are also analyzed. The spectral method is chosen for its ability to describe interface phenomenon. This boundary integral method, developed by Geubelle and Rice (1995) and extended to bimaterial problems by Breitenfeld and Geubelle (1998) and Geubelle and Breitenfeld (1997), allows for the efficient modeling of dynamic debonding using a discretization limited to the interface, thereby providing fine level of discretization, unattainable with more conventional methods such as the finite-element and finite-difference schemes. Interpenetration is prevented at the interface by a contact model with friction being governed by a regularized Coulomb law.

The geometry of our dynamic fracture problem is described in Sect. 2, while the numerical method is presented in Sect. 3. The failure event is studied in Sect. 4 along an Aluminum–Homalite interface through space-time diagrams, the evolution of damage parameters at discrete positions in the path of the crack, energetic arguments, and the evolution of the speed of the leading and trailing edges of the cohesive and contact zones. The influences of the loading conditions in Sect. 5, as well as the material mismatch in Sect. 6, are discussed with the intention to define criteria describing the behavior of different bimaterial situations.

2 Problem description

2.1 Geometry and elastodynamics

The problem geometry is described by two semi-infinite bodies bonded together along a planar interface. Each body is made of a linear isotropic elastic material characterized by the elastic modulus E, the Poisson's ratio ν, the shear wave speed c_s and the dilatational wave speed c_p. In plane strain state, the wave speeds are related to material properties by

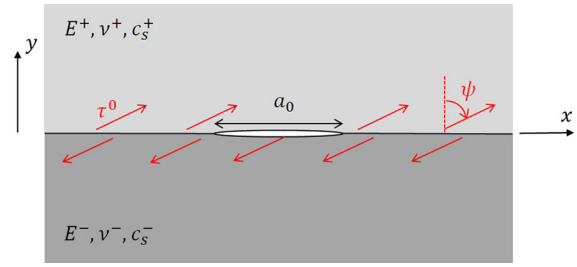

Fig. 1 Geometry of the dynamic fracture problem

$$c_\mathrm{s} = \sqrt{\frac{E}{2\rho(1+\nu)}}, \quad c_\mathrm{p} = \sqrt{\frac{2(1-\nu)}{1-2\nu}}\, c_\mathrm{s} = \eta\, c_\mathrm{s}, \quad (1)$$

where η is the dilatational to shear wave speed ratio. By convention, the top material is defined as the stiffer material. The indices $\pm$ differentiate respectively the top and bottom materials. The bonds at the interface are defined by a fracture toughness G_c. Let a Cartesian system be defined such as y is the normal to the fracture plane. The interface is pre-stressed with a load τ_0 applied in the $x-y$ plane with an angle ψ with respect to the y axis. At time $t = 0$, a crack of initial length a_0 is introduced and starts to propagate along the interface. Figure 1 illustrates the geometry of the problem.

This fracture problem is described by the elastodynamics wave equations with the two in-plane components of the displacement field u_i defined as

$$u_1(\alpha, t) = \phi_{,x} + \vartheta_{,y}, \quad u_2(\alpha, t) = \phi_{,y} - \vartheta_{,x}, \quad (2)$$

where $()_{,i}$ is defined as $\partial/\partial x_i$. ϕ and ϑ are potentials satisfying

$$c_\mathrm{p}^2 \phi_{,\alpha\alpha} = \phi_{,tt}, \quad c_\mathrm{s}^2 \vartheta_{,\alpha\alpha} = \vartheta_{,tt}. \quad (3)$$

2.2 Interface laws

In addition to the continuum model, the problem is described by two interface laws. First, the failure of the interface bonds is described by a rate-independent model which couples normal and shear decohesion. The normal/shear strength of the bonds $\tau_{\mathrm{n,s}}^{\mathrm{str}}$ is related to the associated normal/shear opening of the interface $\delta_{\mathrm{n,s}}$ as

$$\tau_{\mathrm{n,s}}^{\mathrm{str}} = \tau^{\max} \left\langle 1 - \sqrt{(\delta_n/\delta^c)^2 + (\delta_\mathrm{s}/\delta^c)^2} \right\rangle, \quad (4)$$

with $\langle x \rangle = x$ if $x > 0$ and 0 otherwise and where the opening at the interface is defined by the displacement discontinuities,

$$\delta_j(x,t) \equiv u_j(x,0^+,t) - u_j(x,0^-,t). \tag{5}$$

In Eq. (4), $\tau^{\max}$ and δ^c describe the parameters of this cohesive model reducing for a pure mode-I or mode-II failure to a linear law with fracture toughness $G_c = 0.5\,\tau^{\max}\,\delta^c$. In perfect mixed-mode failure, the fracture toughness increases to $\sqrt{2}G_c$. After failure, the faces of the interface may come in contact again with a local compressive stress at the interface $\sigma_{22}(x,0,t) < 0$. In this case, a shear strength due to friction is observed. A Coulomb friction law is used hereafter as

$$\tau_s^{\text{str}} = f|\tilde{\sigma}_{22}|, \tag{6}$$

where $\tilde{\sigma}_{22}$ corresponds to the regularized contact pressure and f is the coefficient of friction. To avoid ill-posedness of the friction problem, a simplified Prakash regularization is considered (Prakash 1998). Since the regularizing effect is directly related to the contact pressure, Rubin and Ampuero (2007) suggested to regularize directly the later instead of the shear strength. Similarly to this approach, we applied the following simplified regularization to the contact pressure:

$$\frac{\mathrm{d}\tilde{\sigma}_{22}}{\mathrm{d}t} = -\frac{1}{t^*}(\tilde{\sigma}_{22} - \sigma_{22}), \tag{7}$$

where t^* is the regularization parameter set as $t^* = 10 \cdot \Delta t$ to satisfy the convergence criteria. More details about the convergence of regularized friction are given in Kammer et al. (2014).

2.3 Material properties

We study dynamic fracture problems along an interface between two materials with an important mismatch. The Aluminum–Homalite interface is chosen to match the experiments of Samudrala and Rosakis (2003). The material properties used in our simulations are presented in Table 1.

Note that index '±' can be interchanged hereafter with 'Al' or 'H', the two components of the bimaterial system. The interface is described by $\tau^{\max} = 5\,\text{MPa}$ and $\delta^c = 0.02\,\text{mm}$, which yields an interface fracture toughness of $G_c = 50\,\text{J/m}^2$. After failure, the coefficient of friction of the interface is set as $f = 0.25$.

Table 1 Material properties

	Aluminum	Homalite
Young's modulus E (GPa)	71	5.3
Poisson's ratio ν (−)	0.33	0.35
Shear wave speed c_s (m/s)	3,100	1,263

3 Numerical method

The dynamic fracture problem is solved with a spectral formulation of the elastodynamic equations. The spectral scheme is based on a spatial Fourier representation of the tractions τ_j and their corresponding displacements u_j at the interface. The tractions are related to Cauchy stresses σ_{ij} by

$$\tau_j(x,t) \equiv \sigma_{2j}(x,0,t). \tag{8}$$

For a two-dimensional propagation, only one spectral component is examined in Eqs. (2)–(3), such that

$$[\phi(\alpha,t), \vartheta(\alpha,t)] = e^{iqx}\,[\Phi(y,t,q), \Theta(y,t,q)]\,. \tag{9}$$

A detailed description of the steps leading to the spectral formulation are given by Geubelle and Rice (1995) for two and three-dimensional problems and by Morrissey and Geubelle (1997) for mode-III problems.

The independent spectral formulation described by Breitenfeld and Geubelle (1998) and Geubelle and Breitenfeld (1997) is chosen in this paper. In this approach, both half-spaces can be modeled separately before applying the interface conditions, leading to more precision and stability for 2-D in-plane problems (Breitenfeld and Geubelle 1998). This formulation gives the following elastodynamic equations.

$$\tau_j(x,t) = \tau_j^0(x,t) - V_{jk}^{\pm}\frac{\partial u_k^{\pm}(x,t)}{\partial t} + f_j^{\pm}(x,t). \tag{10}$$

In Eq. (10), τ_j^0 corresponds to the projection of the external loading of Fig. 1 and denotes the tractions present at the interface in the absence of any debonding. The additional terms in Eq. (10) are associated with the presence of displacement discontinuities along the

fracture plane. V_{jk} represents a diagonal matrix constructed with the shear modulus $\mu = \frac{E}{2(1+\nu)}$ and the ratio η of P-wave over S-wave speed (cf. Eq. 1) as

$$V_{11} = \mu/c_s, \quad V_{22} = \eta\mu/c_s. \tag{11}$$

The second term on the right hand side of (10) corresponds to the instantaneous response, while the third term, $f_j^{\pm}(x,t)$, represents the effect of the slip history. This component of the interface tractions is evaluated in the Fourier space as a convolution over the past slip history. For a given time t and spectral mode q, it is expressed as

$$\begin{aligned}
&F_1^{\pm}(t;q) \\
&= \mp\mu^{\pm}|q| \int_0^t H_{11}^{\pm}\left(|q|c_s^{\pm}t'\right) U_1^{\pm}(t-t';q)|q|c_s^{\pm}\mathrm{d}t' \\
&\quad + i\mu^{\pm}q \int_0^t H_{12}^{\pm}\left(|q|c_s^{\pm}t'\right) U_2^{\pm}(t-t';q)|q|c_s^{\pm}\mathrm{d}t' \\
&\quad + i(2-\eta^{\pm})\mu^{\pm}qU_2^{\pm}(t;q), \\
&F_2^{\pm}(t;q) \\
&= \mp\mu^{\pm}|q| \int_0^t H_{22}^{\pm}\left(|q|c_s^{\pm}t'\right) U_2^{\pm}(t-t';q)|q|c_s^{\pm}\mathrm{d}t' \\
&\quad - i\mu^{\pm}q \int_0^t H_{12}^{\pm}\left(|q|c_s^{\pm}t'\right) U_1^{\pm}(t-t';q)|q|c_s^{\pm}\mathrm{d}t' \\
&\quad - i(2-\eta^{\pm})\mu^{\pm}qU_1^{\pm}(t;q).
\end{aligned} \tag{12}$$

where F_j and U_j are the Fourier coefficients of f_j and u_j respectively. $H_{ij}(T)$ denote the convolution kernels which are given in Breitenfeld and Geubelle (1998). Figure 2 illustrates the shapes of the different kernels for a material with $\nu = 0.35$.

Finally, continuity of displacements and tractions through the interface yields the element velocities $\dot{u}_j^{\pm}$ which are expressed as

$$\left(\tau_{n,s}^{str} > \tau_{2,1}\right) \begin{cases} \dot{u}_1^+ = \dot{u}_1^- = \frac{c_s^+}{\mu^+}\left(\frac{f_1^+ - f_1^-}{1+\frac{\xi}{\zeta}}\right) \\ \dot{u}_2^+ = \dot{u}_2^- = \frac{c_s^+}{\mu^+}\left(\frac{f_2^+ - f_2^-}{\eta^+ + \frac{\xi}{\zeta}\eta^-}\right) \end{cases}, \tag{13}$$

$$\left(\tau_{n,s}^{str} \le \tau_{2,1}\right) \begin{cases} \dot{u}_1^{\pm} = \pm c_s^{\pm}\left(\frac{\tau_1^0 + f_1^{\pm} - \tau_s^{str}}{\mu^{\pm}}\right) \\ \dot{u}_2^{\pm} = \pm c_s^{\pm}\left(\frac{\tau_2^0 + f_2^{\pm} - \tau_n^{str}}{\mu^{\pm}\eta^{\pm}}\right) \end{cases}, \tag{14}$$

where $\xi = c_s^+/c_s^-$ and $\zeta = \mu^+/\mu^-$.

In the case of possible overlapping of the crack faces Eq. (14) are adapted to ensure the vanishing of the normal displacement. The normal motion is modified as

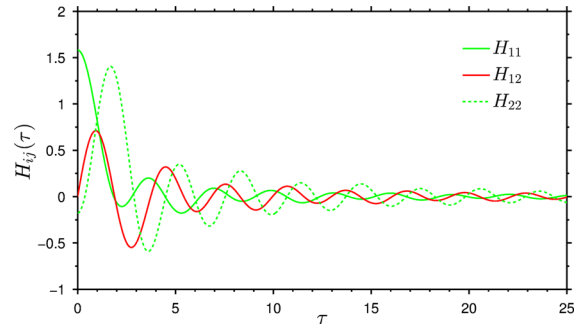

Fig. 2 Convolution kernels applied in the spectral formulation ($\nu = 0.35$)

$$\begin{aligned}
\dot{u}_2^+ &= \frac{c_s^+}{\eta^+ + \frac{\xi\eta^-}{\zeta}}\left[\frac{\tau_2^+ - \tau_2^-}{\mu^+} - \frac{\xi\eta^-}{\zeta}\left(\frac{u_2^+ - u_2^-}{c_s^+\Delta t}\right)\right], \\
\dot{u}_2^- &= \dot{u}_2^+ + \frac{u_2^+ - u_2^-}{\Delta t}.
\end{aligned} \tag{15}$$

This modification generates a compressive stress at the interface,

$$\hat{\tau}_2 = \tau_2^+ - \eta^+\mu^+\frac{\dot{u}_2^+}{c_s^+}. \tag{16}$$

The shear motion is still governed by (14), with the associated strength τ_s^{str} due to friction at the interface and given by the chosen friction model (6).

4 Reference case ($\psi = 75°$)

The dynamic debonding along an Aluminum–Homalite interface obtained for a shear-dominated loading is described in detail in this section. The material properties of each medium and the interface were defined in Sect. 2.3. Since it is based on a Fourier series representation of the solution, the spectral scheme introduces a spatial period X. A $X = 1$ m domain pre-stressed with an in-plane uniform load of $\tau_0/\tau^{max} = 0.6$ is investigated. The in-plane loading angle is set at $\psi = 75°$.

At time $t = 0$, an initial crack of size $a_0/X = 0.05$ is introduced at the center of the domain and starts to propagate in both directions. For simplicity and efficiency of the Fourier transform between spatial and spectral domains, the number of grid points is usually chosen as a power of 2. The interface is discretized with 4,096 elements, resulting in an element size of $\Delta x = 0.24$ mm. The time step is set by the parameter β corresponding to the fraction of one grid spacing traveled by a shear wave in the stiffer material,

$$\Delta t = \beta \frac{\Delta x}{c_{\mathrm{s}}^{+}}. \tag{17}$$

Breitenfeld and Geubelle (1998) showed that a value of $\beta = 0.4$ guarantees a good stability of the solution. This value is therefore adopted in the simulations presented hereafter. A convergence study validates the choice of the grid spacing and time step values.

4.1 Evolution of cohesive and contact zones

Figure 3 shows a space–time representation of the crack propagation. The mismatch between the top and bottom materials causes different failure behaviors for the two directions of propagation. Asymmetry in the crack growth was also recorded experimentally for a centered crack growing under a mixed-mode loading (Xia et al. 2008). On the left side, a contact area appears and directly trails the crack tip throughout the simulation. On the right side, a friction zone also trails the crack tip for a while but quickly detaches. As the simulation goes on, the size of this frictional contact area decreases before the contact zone completely vanishes. Those two distinct behaviors are in good agreement with the different types of contact zones assessed in the experimental work of Samudrala and Rosakis (2003). To confirm that the two behaviors are clearly different, the simulation duration was extended showing that the left friction area does not detach from the crack tip. The study of the crack and contact zone velocity profiles (Fig. 4) also highlights two different regimes.

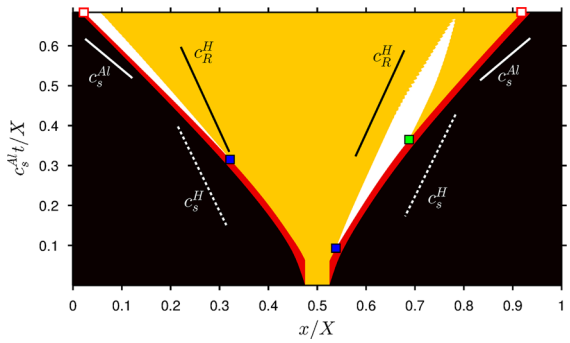

Fig. 3 Space–time diagram of a dynamic debonding between Aluminum and Homalite for $\psi = 75°$. The *black* regions correspond to intact portions of the interface, the *dark gray* areas (*red online*) indicate the cohesive zones, the *light gray* regions (*yellow online*) are traction-free and the *white* regions correspond to the contact zones. *Squares* highlight measurement points for which the propagation speed is reported in Fig. 9

In the left direction (Fig. 4a), friction appears at intersonic propagation speed, around $0.75c_{\mathrm{s}}^{\mathrm{Al}} \simeq 1.84c_{\mathrm{s}}^{\mathrm{H}}$. At the end of the simulation, the crack propagation reaches a quasi steady state and the friction zone continues to grow.

On the right side (Fig. 4b), the contact zone appears when the crack propagates in the unfavorable speed range as defined by Liu et al. (1995), i.e., between $c_{\mathrm{s}}^{\mathrm{H}}$ and $\sqrt{2}c_{\mathrm{s}}^{\mathrm{H}}$. As the propagation speed continues to increase and leaves the unstable range, the contact area decreases in size and eventually vanishes completely. This observation is in agreement with the asymptotic model derived by Liu et al. (1995), which predicts a crack face closure only at this unfavorable velocity regime.

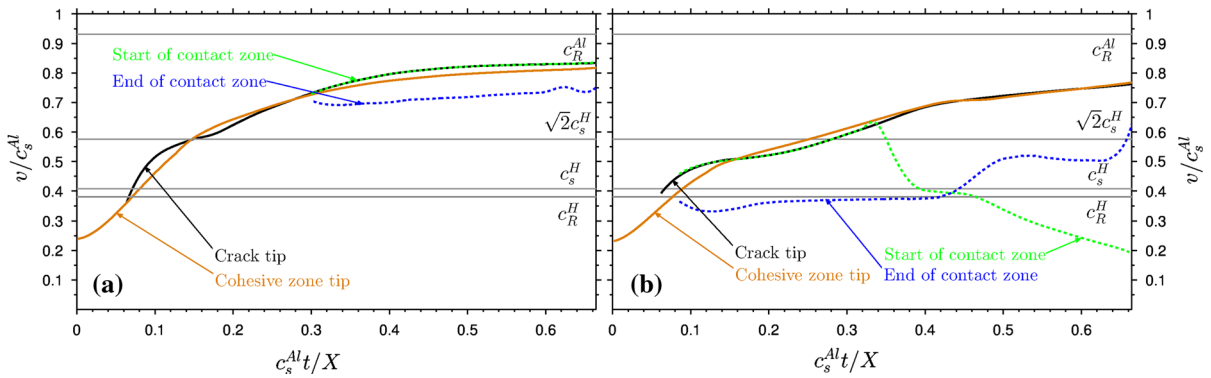

Fig. 4 Evolution over time of the propagation speed of the cohesive and contact zones for the left (**a**) and right (**b**) debonding path under $\psi = 75°$

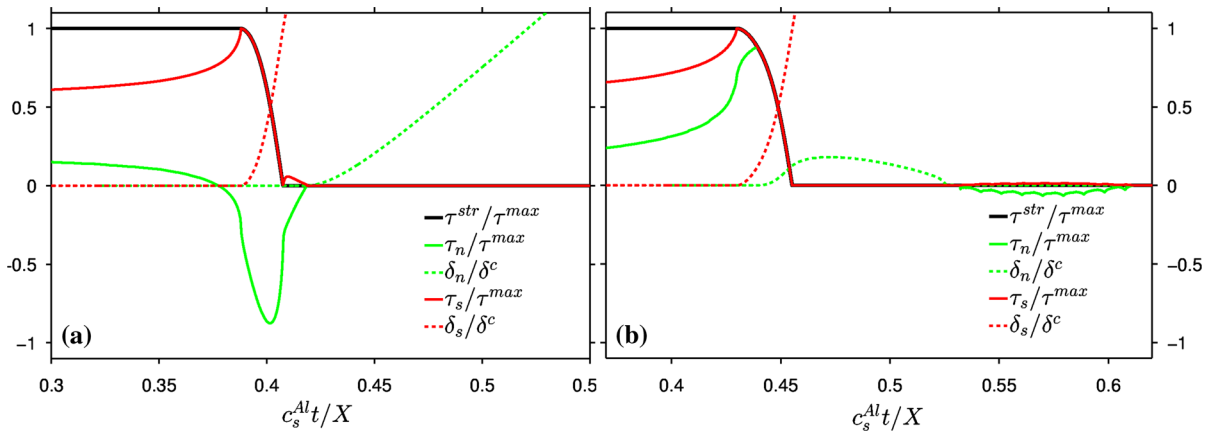

Fig. 5 Evolution of the cohesive strength, normal and shear tractions and displacement jumps at $x/X = 0.25$ (**a**) and at $x/X = 0.75$ (**b**) with $\psi = 75°$

4.2 Failure process

Figure 5 compares the history of interface points located in the path of the left-propagating and right-propagating debonding fronts.

As the crack tip approaches the point of observation, a stress concentration is observed in the shear and normal directions. On both sides, failure is initiated in shear due to the shear-dominated nature of the loading. The key difference is the traction behavior in the normal direction. For the left side, the normal traction is in compression. Thereby, the failure is in pure shear. The concentration in compression explains that the two faces are in contact just after failure. Inversely, the concentration of normal stress comes up in tension for the right side. In this case, the normal stress curve also intercepts the strength curve and the debonding is a mixed-mode failure. Because the interface is under tension, the crack face opens after failure. However, after a certain amount of time, a closure motion brings both faces in contact. This delayed contact corresponds to the region with a detached friction area in Fig. 3. This particular effect indicates that a closure wave propagating at the Homalite surface causes this detached friction area. The propagation speed of the trailing end of the detached contact zone is close to $c_{\mathrm{R}}^{\mathrm{H}}$ as shown in Fig. 4b and sustains the assumption of a surface-level perturbation. A similar disturbance traveling at the Rayleigh wave velocity of the more compliant material is described in the experiments of Singh and Shukla (cf. Fig. 4b compared to Fig. 12 in Singh and Shukla 1996).

4.3 Energetics

Finally, the evolution of the effective fracture toughness $\mathrm{d}E/\mathrm{d}A$ is computed during the simulation, where E denotes the energy and A represents the debonded area. The effective fracture toughness is then directly related to v, the crack propagation speed as

$$\Gamma = \frac{\mathrm{d}E}{\mathrm{d}A} = \frac{\mathrm{d}E}{\mathrm{d}t}\frac{1}{v} = \frac{\dot{E}}{v}. \tag{18}$$

During the failure process, energy is dissipated in the cohesive zone by debonding and in the contact zone by friction as

$$\begin{aligned}
\dot{E}_n(t) &= \int_{\text{cohesive zone}(t)} \tau_n^{\mathrm{str}}(x,t)\dot{\delta}_n(x,t)\mathrm{d}x,\\
\dot{E}_{\mathrm{s}}(t) &= \int_{\text{cohesive zone}(t)} \tau_{\mathrm{s}}^{\mathrm{str}}(x,t)\dot{\delta}_{\mathrm{s}}(x,t)\mathrm{d}x,\\
\dot{E}_f(t) &= \int_{\text{contact zone}(t)} f|\tilde{\tau}_n|\dot{\delta}_s(x,t)\mathrm{d}x.
\end{aligned} \tag{19}$$

Figure 6 presents the evolution of the fracture toughness normalized by the reference fracture toughness G_c, which is the energy dissipated in a pure mode (I or II) failure. Shear failure process is predominant (see Fig. 6b), as expected for this intersonic crack. With the same numerical method, Geubelle and Kubair (2001) showed that intersonic debonding along a single-material interface is purely driven by shear. Nevertheless, two additional features are observed with this bimaterial situation. First, the effective fracture toughness is significantly higher than G_c because of

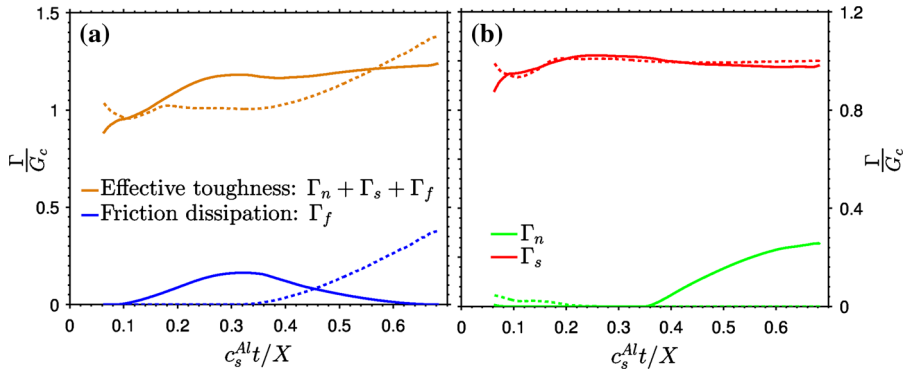

Fig. 6 Evolution of the effective fracture toughness and its different components, i.e., the dissipation by friction Γ_f and by tensile Γ_n and shear Γ_s debonding, for the left (*dashed lines*) and right (*full lines*) paths with $\psi = 75°$

the friction-induced dissipation. Figure 6a presents values of Γ_f up to $0.4\,G_c$. It might even exceeds $0.7\,G_c$ by increasing the coefficient of friction up to $f = 0.8$. Therefore the presence of a contact zone along the interface plays an important role in failure energetics. Second, in bimaterial set-ups, mixed mode failure occurs also for intersonic cracks, which was shown to be impossible along single-material interfaces (Broberg 1989; Geubelle and Kubair 2001). In Fig. 6b, mode-I failure process is observed after $c_\mathrm{s}^\mathrm{Al}t/X = 0.36$ as soon as the contact zone detaches from the right tip.

5 Influence of loading angle ψ

In this section, we investigate the effect of the loading condition by reproducing the reference set-up with different values of ψ between 0° and 90°.

5.1 Evolution of cohesive and contact zones

For a pure far field tensile loading, i.e $\psi = 0°$, the crack propagation is perfectly symmetric and no contact area is observed in both directions of propagation. Each crack tip propagates at a subsonic speed close to c_R^H, as a sufficient amount of shear is needed to allow intersonic propagations (Geubelle and Kubair 2001). Adding shear to the far field loading ($\psi > 0°$) has two effects. First, the shear stress becomes more prominent and results in higher crack speeds. Secondly, the symmetry is broken and the two propagation paths present different behaviors, as shown in Fig. 7 for $\psi = 50°$. On the right path, the crack accelerates progressively, while the left tip stays almost at a constant speed close to c_R^H before jumping suddenly to intersonic velocities.

This sharp transition is also observable on the velocity profile at about $c_\mathrm{s}^\mathrm{Al}t/X = 0.45$ in Fig. 8a, where the

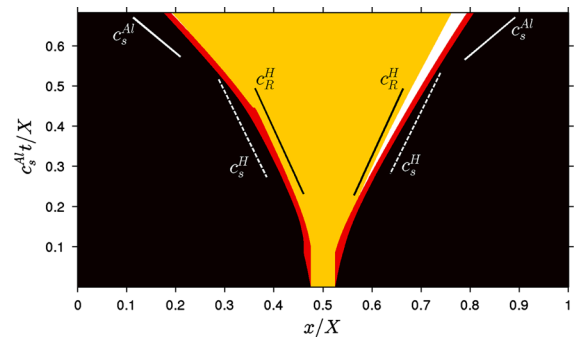

Fig. 7 Space–time diagram of dynamic debonding between Aluminum and Homalite for $\psi = 50°$ illustrating subsonic/intersonic transition for both directions. (*Colour code* as in Fig. 3)

left tip jumps directly from c_R^H to a speed above $\sqrt{2}c_\mathrm{s}^\mathrm{H}$. This sharp behavior causes the singularity observed in Fig. 8a. At the end of the simulation, a thin contact zone appears directly behind the left tip. The right crack tip accelerates continuously up to the intersonic regime and a contact zone develops as soon as it exceeds c_s^H (see Fig. 8b). Unlike the $\psi = 75°$ configuration (Fig. 4b), the right tip never exceeds $\sqrt{2}c_\mathrm{s}^\mathrm{H}$ and the contact zone does not detach from the tip.

We have considered different values of ψ between 0° and 90°. A summary of the velocity profiles (i.e., the crack speed when contact appears behind the tip, as the contact zone detaches and at the end of the simulation) is presented in Fig. 9. As observed before, with normal-dominated loading conditions, the crack propagates at sub-Rayleigh speed and no contact is observed at the interface. As the loading conditions go from pure tensile ($\psi = 0°$) to pure shear ($\psi = 90°$), the propagation speed and the asymmetry increase. The difference between each side of propagation can be characterized in two distinct ways. First, the subsonic/intersonic

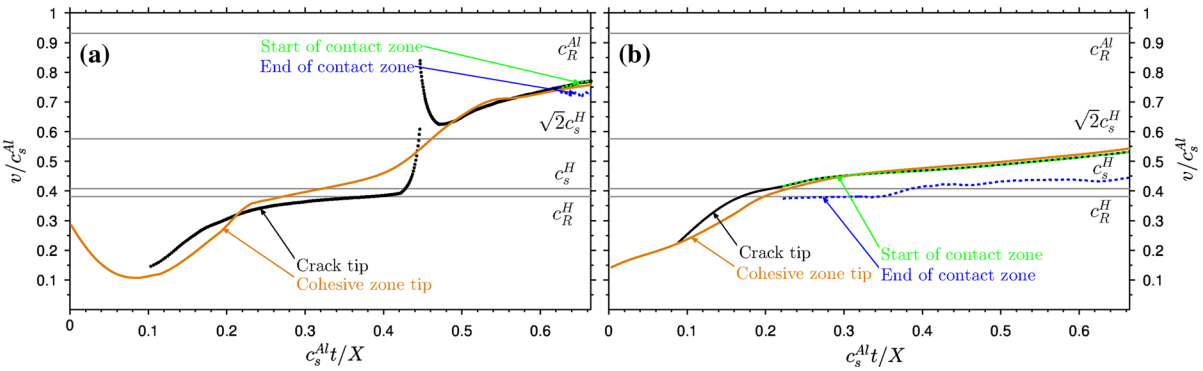

Fig. 8 Evolution of the propagation speed of the cohesive and contact zones for the left (**a**) and right (**b**) debonding path under $\psi = 50°$

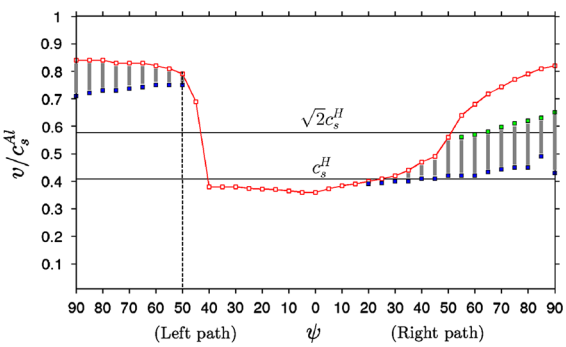

Fig. 9 Influence of ψ on the propagation speed v. As illustrated in Fig. 3, *red squares* show the propagation velocities reached at the end of the simulation, *black* (*blue online*) *squares* the speeds when a contact area appears behind the crack tip and *gray* (*green online*) *squares* the speeds when the contact zone detaches from the crack tip. The *vertical gray bars* highlight crack velocities where the contact zone is trailing the crack tip. The *vertical dashed line* represents the abscissa of Fig. 10

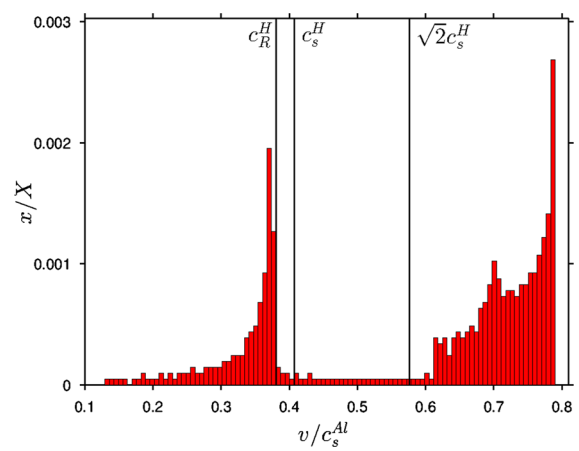

Fig. 10 Histogram of the crack velocities as function of the distance traveled for $\psi = 50°$ on the *left side* showing the existence of a forbidden velocity regime between c_R^H and $\sqrt{2}c_s^H$. The abscissa of the histogram corresponds to the dashed line in Fig. 9

transition is clearly different. In the left direction, the crack has only two regimes of propagation: a subsonic steady state close to c_R^H for $\psi \leq 40°$ and an intersonic at about 0.8 c_s^{Al} for higher ψ. Between these velocities, the transition is sharp and sudden. The unfavorable range is a forbidden region of propagation, as illustrated in Fig. 10 which presents the histogram of left crack speeds recorded with $\psi = 50°$. Similar behavior were observed in the experiments of Lambros and Rosakis (1995) where the crack stayed at a speed just below c_s^H for a while before accelerating rapidly above $\sqrt{2}c_s^H$. On the right side of the domain, the subsonic/intersonic transition is smooth and progressive.

The behavior of contact is the second clear difference between left and right crack propagation directions. In the left direction, contact zones appear with intersonic propagation speed, around 0.75 c_s^{Al}. The emergence of this friction zone coincides with the end of crack acceleration. In the right direction, Fig. 9 confirms that contact areas are directly related to a propagation at unfavorable speeds. As the crack moves faster than $\sqrt{2}c_s^H$, the contact zone detaches from the crack tip and eventually fully vanishes. Before detaching, the trailing end of this contact zone is propagating at the Rayleigh wave speed of Homalite (cf Fig. 4b).

5.2 Impact of ψ on the failure process

A characteristic feature of bimaterial interface failure is the inherent mode mixity of the failure process, even under pure far-field loading conditions ($\psi = 0°$ or

$\psi = 90°$). Bimaterial conditions break the symmetry at the interface and the direction of principal stresses are not perpendicular anymore to the interface. The presence of both shear and normal stresses at crack tips of pure tensile and shear loadings is shown in Fig. 11.

The comparison of failure processes between shear and tensile loading conditions explains the asymmetric behavior observed in Fig. 9 between left and right propagating fronts. The stress field at the right tip has similar patterns under $\psi = 0°$ and $\psi = 90°$, i.e positive values for normal and shear stresses. In the left direction, the stress field presents a different pattern between $\psi = 0°$ and $\psi = 90°$, with both components changing sign. The sharp transition observed in Fig. 9 is therefore explained by the fact that the crack changes its regime of propagation as the loading condition goes from tensile to shear.

The same analysis explains the subsonic/intersonic transition under a fixed value of ψ. Figure 12 compares the stress profiles measured for a subsonic and an intersonic crack propagation under $\psi = 50°$. At subsonic speeds, the normal stress close to the tips is tensile and contributes to the cohesive failure. At intersonic speeds, the normal stress at the left tip changes sign and is now compressive. This drastic change in the failure pattern associated to the sharp jump in the velocity profile corresponds to a subsonic/intersonic transition similar to the Burridge–Andrews mechanism (Burridge 1973; Andrews 1976). This transition, initially described for shear cracks along frictional interfaces, occurs through the nucleation of an intersonic daughter crack in front of the main rupture. Coker et al. (2003) gave the first experimental observation of this transition mechanism along a composite-Homalite interface. Geubelle and Kubair (2001) as well as Liu and Lapusta (2008) observed similar intersonic daughter cracks with the spectral boundary integral method. Figure 13 presents the evolution of mode mixity evaluated through the energy dissipated during bonds failure as function of the propagation speed. In the left direction (Fig. 13a), the existence of two distinct regimes of propagation are identified between sub-Rayleigh and intersonic speeds separated by spaced out dots at forbidden velocities (also observed at the singularity in

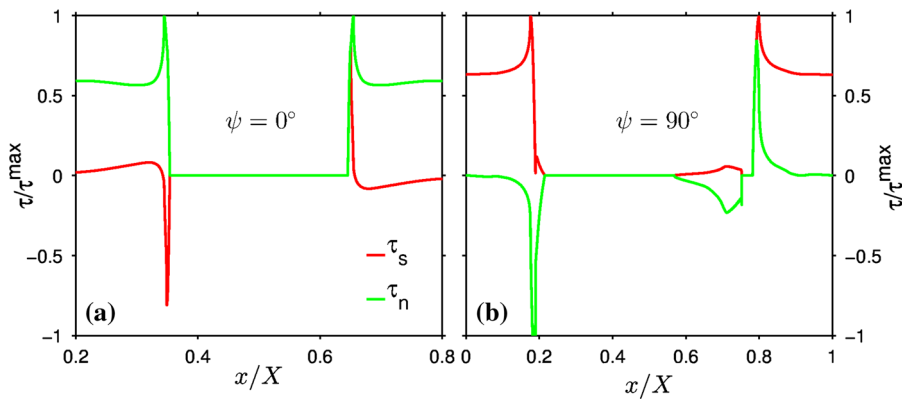

Fig. 11 Normal and shear stress profiles at $t = 0.48\, c_s^{Al} t/X$ along the interface for $\psi = 0°$ and $\psi = 90°$. Along bimaterial interfaces, mixed-mode stress fields at the crack tip are observed even under pure tensile and shear far-field loadings

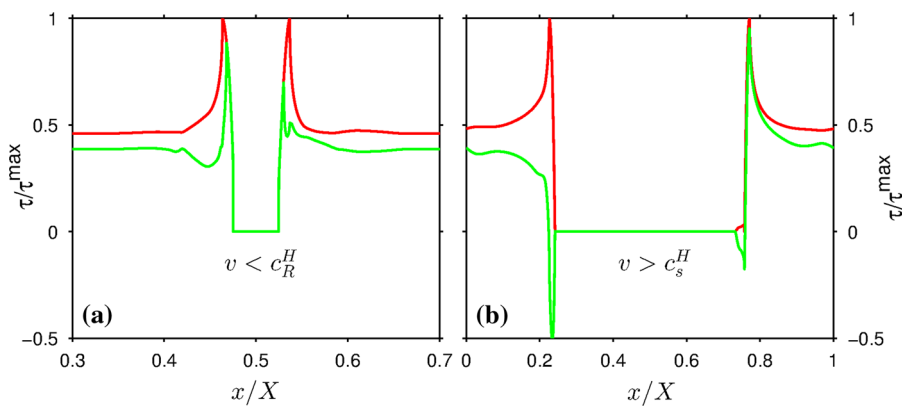

Fig. 12 Normal and shear stress profiles along the interface for subsonic ($t = 0.07\, c_s^{Al} t/X$) and intersonic ($t = 0.62\, c_s^{Al} t/X$) crack growth under $\psi = 50°$

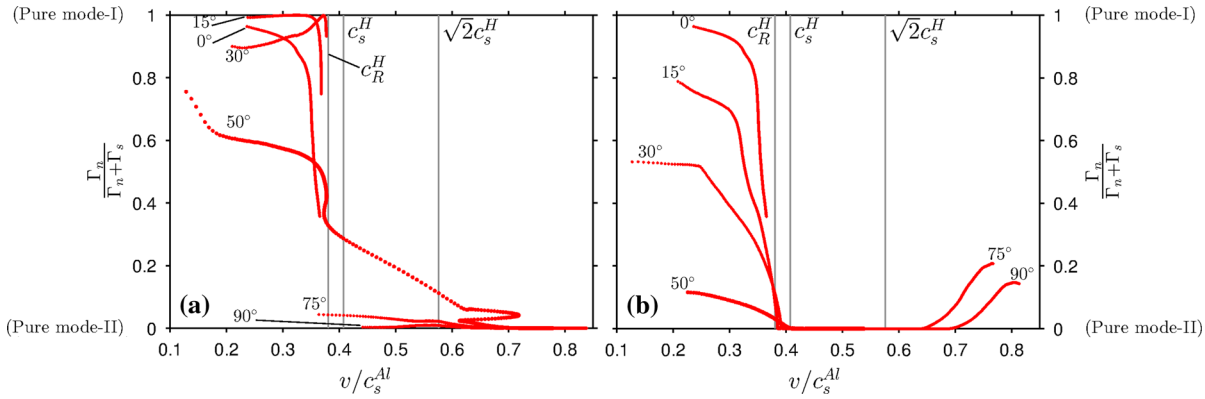

Fig. 13 Evolution of the ratio of energy dissipated by mode-I failure over the total energy dissipated in cohesive zones as function of the crack velocity for different values of ψ, at the left (**a**) and right (**b**) crack fronts

Fig. 8a). While mixed mode failure is observed in the subsonic regime, intersonic cracks are purely driven by shear and the normal opening only occurs after complete failure of the interface. In the right direction, the subsonic/intersonic transition is smoother (Fig. 13b). As crack closure (in normal direction) is predicted for crack speeds between c_s^H and $\sqrt{2}c_s^H$ (Liu et al. 1995), the energy dissipation by mode-I failure tends to zero when the right front propagates in this regime where a contact zone appears directly behind the tip (Fig. 12b at $x/X = 0.75$). However, once the propagation speed exceeds $\sqrt{2}c_s^H$, mixed mode failure is possible in the right direction. Intersonic cracks driven by both tension and shear are the results of the bimaterial nature of this system and were not observed along single-material interfaces (Broberg 1989; Geubelle and Kubair 2001).

6 Effect of material mismatch

The observed mechanisms of the Aluminium–Homalite problem studied before could be described only by wave speeds of the compliant material (c_s^H, c_R^H) since Aluminium wave speeds are much higher than the crack propagation velocity. In this section, the effect of the material mismatch on the crack behavior is evaluated. Homalite is kept as bottom material, with the properties defined in Sect. 2.3. The top material is only defined by the Young's modulus mismatch E^+/E^H. To simplify the analysis, the Poisson's ratio and the density of the top material are always the same as Homalite. Thereby, the shear wave speed of the top material can directly be computed as

$$c_s^+ = \sqrt{\frac{E^+}{E^H}}\, c_s^H. \tag{20}$$

The fracture toughness of the interface remains the same as in the previous simulations and reference case loading conditions are applied ($\psi = 75°$). With lower mismatch values, the speeds of crack fronts are in the range of top material wave speeds (c_s^+, c_R^+) and crack propagation is described by material properties of both medium. The single-material problem $E^+/E^H = 1$ corresponds to an intersonic pure shear failure without contact along the interface. Under this shear-dominant loading, the crack propagation is characterized by a rapid acceleration up to the steady state velocity close to $v = 1.87c_s^H$. This behavior is consistent with both experimental (Rosakis et al. 1999) and numerical (Geubelle and Kubair 2001) observations of intersonic crack growth along homogeneous interfaces. Similar to the description made on the left region of propagation for the Aluminium–Homalite system, the crack front needs a sufficient amount of energy to become intersonic, otherwise it continues propagating at a sub-Rayleigh velocity. For small values of mismatch, the crack has sufficient energy to accelerate up to intersonic speeds with respect to both materials as illustrated in Fig. 14a. As the mismatch increases, the top material intersonic regime distances itself from the crack velocity range, up to levels unreachable by the crack front. Figure 14b presents this situation for $E^+/E^H = 4$ where the right tip velocity is bonded at $v \leq c_R^+$. It is interesting to note that this behavior related to the left propagation path during Aluminium–Homalite simulations is observed in the right direction while related to

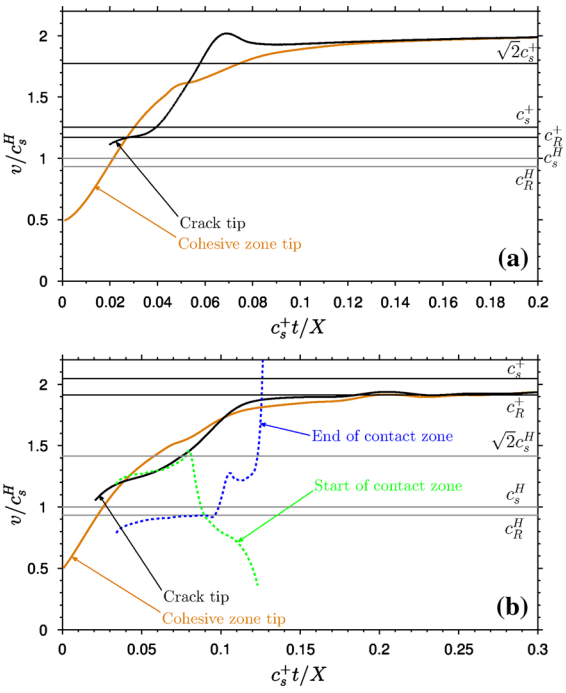

Fig. 14 Evolution of the propagation speed of the cohesive and contact zones of the right front at a bimaterial interface with **a** $E^+/E^{\mathrm{H}} = 1.5$ and **b** $E^+/E^{\mathrm{H}} = 4$

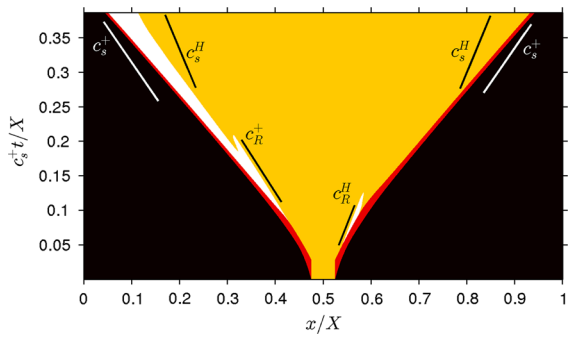

Fig. 15 Space–time diagram of dynamic debonding along a $E^+/E^{\mathrm{H}} = 2.5$ interface under $\psi = 75°$ showing contact behavior related to the *top* and *bottom* wave speeds. (*Colour code* as in Fig. 3)

top material wave speeds. More generally, this behavior is observed in relation with the material whose particle displacements are in the direction of failure propagation. In their experimental and numerical work, Coker et al. (2003) also showed different crack speed regimes as a function of the direction of relative sliding. This observation is also verified in the left path of propagation influenced by top material wave speeds for small mismatches. Indeed, the detached contact zone, observed exclusively in the right direction with an Aluminium–Homalite interface is inverted when it is related to top material wave speeds. As the mismatch increases, the left front propagates through the speed range between c_{s}^+ and $\sqrt{2}c_{\mathrm{s}}^+$ and a detaching contact zone appears in addition to the trailing contact zone (cf. Fig. 15). Thus, a detached contact zone is caused by a Rayleigh disturbance emerging up at the surface of the material whose particle displacements are in the opposite direction compared to the front propagation. This statement is confirmed by the propagation speed of the trailing end of the detached contact zones in Fig. 15 which are c_{R}^+ in the left direction and $c_{\mathrm{R}}^{\mathrm{H}}$ in the right direction.

7 Conclusion

Bimaterial interface fracture has been investigated numerically between two linearly elastic semi-infinite media. The analysis has been conducted using a spectral scheme, which allows for a fine spatial and temporal discretization of the failure process. The objective was to study the subsonic/intersonic transition and to provide a better description of the role of frictional contact in this process.

Compared to the single-material system, the bimaterial set-up breaks the symmetry at the interface causing two effects. First, an inherent mode mixity participates in the failure, even with purely tensile or shear far field loading conditions. Secondly, we observed different crack behaviors at the left and the right tips as function of compliant material wave speeds. By reducing the material mismatch, we showed that the description of the different crack speed regimes is also valid when related to the wave speeds of the stiffer material. Therefore, the crack behavior can be described as function of the front propagation direction with respect to the slip direction of material particles. If the front has the same direction than the particle displacements of the material, a forbidden speed range was observed between c_{R} and c_{s}, forcing the crack to have two distinct regimes of propagation. Either it moves at a sub-Rayleigh speed or, when sufficient energy is available, it jumps to an intersonic regime. This sharp jump and a complete change in the failure stress pattern is caused by the nucleation of a daughter crack in front of the main rupture, similar to the Burridge–Andrews mechanism (Burridge 1973; Andrews 1976). When the front propagates in a direc-

tion opposite to particle displacements of the material, the subsonic/intersonic acceleration is smooth and any speed is admissible in the transition. Nevertheless, in the velocity range $c_s < v < \sqrt{2}c_s$, mode-I failure is forbidden and the faces stay in contact after decohesion. This behavior is consistent with the asymptotic solution of Liu et al. (1995) predicting crack face closure when the crack propagates at these unfavorable velocities.

Particular attention was given to the behavior and the role of frictional contact in bimaterial failures. For this purpose, contact conditions were implemented in the model associated with a regularized Coulomb friction law. Similar to the experiments (Samudrala and Rosakis 2003), two distinct contact behaviors were observed along the interface. At the left tip of cracks subjected to a shear-dominated loading (with stiffer material on top), the material mismatch causes a normal compressive stress leading to a contact zone trailing the crack front. Another type of contact zone was observed as the front propagates with $c_s < v < \sqrt{2}c_s$ with respect to the material whose particle displacements are opposite to the front. Subsequent to face closure behind the crack tip, a Rayleigh disturbance propagating at the surface of the material causes a contact zone detached from the propagation front. The energetic study provided a quantitative description of the effect of friction increasing the effective fracture toughness of the interface, even for small coefficients of friction ($f = 0.25$).

To conclude, with a single set-up our study allows for the simulations and the descriptions of many different behaviors observed experimentally (distinct natures of contact zones, unfavorable velocity range, asymmetric crack propagation). Our analysis was verified by changing the loading conditions as well as the material mismatch at the interface confirming the applicability of the proposed criteria to the description of different bimaterial situations as well as the single-material set-up.

Acknowledgments Most of this work was performed during F. Barras' internship in the Aerospace Engineering Department at the University of Illinois. The support of the European Research Council (ERCstg UFO-240332) is gratefully acknowledged.

References

Andrews DJ (1976) Rupture velocity of plane strain shear cracks. J Geophys Res 81(32):5679–5687

Breitenfeld MS, Geubelle PH (1998) Numerical analysis of dynamic debonding under 2D in-plane and 3D loading. Int J Fract 93(1–4):13–38

Broberg KB (1989) The near-tip field at high crack velocities. Int J Fract 39(1–3):1–13

Burridge R (1973) Admissible speeds for plane-strain self-similar shear cracks with friction but lacking cohesion. Geophys J R Astron Soc 35(4):439–455

Coker D, Rosakis AJ (2001) Experimental observations of intersonic crack growth in asymmetrically loaded unidirectional composite plates. Philos Mag A 81(3):571–595

Coker D, Rosakis A, Needleman A (2003) Dynamic crack growth along a polymer composite-Homalite interface. J Mech Phys Solids 51(3):425–460

Freund LB (1979) The mechanics of dynamic shear crack propagation. J Geophys Res Solid Earth 84(B5):2199–2209

Freund LB (1990) Dynamic fracture mechanics. Cambridge University Press, Cambridge

Geubelle PH, Rice JR (1995) A spectral method for three-dimensional elastodynamic fracture problems. J Mech Phys Solids 43(11):1791–1824

Geubelle PH, Breitenfeld MS (1997) Numerical analysis of dynamic debonding under anti-plane shear loading. Int J Fract 85(3):265–282

Geubelle PH, Kubair DV (2001) Intersonic crack propagation in homogeneous media under shear-dominated loading: numerical analysis. J Mech Phys Solids 49(3) :571–587

Hao S, Liu WK, Klein PA, Rosakis AJ (2004) Modeling and simulation of intersonic crack growth. Int J Solids Struct 41(7):1773–1799

Huang Y, Wang W, Liu C, Rosakis AJ (1998) Intersonic crack growth in bimaterial interfaces: an investigation of crack face contact. J Mech Phys Solids 46(11):2233–2259

Kammer DS, Yastrebov V, Spijker P, Molinari JF (2012) On the propagation of slip fronts at frictional interfaces. Tribol Lett 48(1):27–32

Kammer DS, Yastrebov VA, Anciaux G, Molinari JF (2014) The existence of a critical length scale in regularised friction. J Mech Phys Solids 63:40–50

Kubair DV, Geubelle PH, Huang Y (2002) Intersonic crack propagation in homogeneous media under shear-dominated loading: theoretical analysis. J Mech Phys Solids 50(8):1547–1564

Lambros J, Rosakis AJ (1995) Shear dominated transonic interfacial crack growth in a bimaterial-I. Experimental observations. J Mech Phys Solids 43(2):169–188

Liu C, Huang Y, Rosakis AJ (1995) Shear dominated transonic interfacial crack growth in a bimaterial-II. Asymptotic fields and favorable velocity regimes. J Mech Phys Solids 43(2):189–206

Liu Y, Lapusta N (2008) Transition of mode II cracks from sub-Rayleigh to intersonic speeds in the presence of favorable heterogeneity. J Mech Phys Solids 56(1):25–50

Morrissey JW, Geubelle PH (1997) A numerical scheme for mode III dynamic fracture problems. Int J Numer Methods Eng 40(7):1181–1196

Needleman A (1999) An analysis of intersonic crack growth under shear loading. J Appl Mech 66(4):847–857

Needleman A, Rosakis AJ (1999) The effect of bond strength and loading rate on the conditions governing the attainment

of intersonic crack growth along interfaces. J Mech Phys Solids 47(12):2411–2449
Prakash V (1998) Frictional response of sliding interfaces subjected to time varying normal pressures. J Tribol 120(1):97–102
Rosakis AJ, Samudrala O, Singh RP, Shukla A (1998) Intersonic crack propagation in bimaterial systems. J Mech Phys Solids 46(10):1789–1813
Rosakis AJ, Samudrala O, Coker D (1999) Cracks faster than the shear wave speed. Science 284(5418):1337–1340
Rosakis AJ (2002) Intersonic shear cracks and fault ruptures. Adv Phys 51(4):1189–1257
Rubin AM, Ampuero JP (2007) Aftershock asymmetry on a bimaterial interface. J Geophys Res Solid Earth 112(B5):B05,307
Samudrala O, Rosakis AJ (2003) Effect of loading and geometry on the subsonic/intersonic transition of a bimaterial interface crack. Eng Fract Mech 70(2):309–337
Singh RP, Shukla A (1996) Subsonic and intersonic crack growth along a bimaterial interface. J Appl Mech 63(4):919–924
Singh RP, Lambros J, Shukla A, Rosakis AJ (1997) Investigation of the mechanics of intersonic crack propagation along a bimaterial interface using coherent gradient sensing and photoelasticity. Proc R Soc Lond Ser A Math Phys Eng Sci 453(1967):2649–2667
Xia KW, Rousseau CE, Rosakis AJ (2008) Experimental investigations of spontaneous bimaterial interfacial fractures. J Mech Mater Struct 3(1):173–184
Xu XP, Needleman A (1996) Numerical simulations of dynamic crack growth along an interface. Int J Fract 74(4):289–324